Optical Scattering from Isolated Metal Nanoparticles and Arrays

Gregory A. Wurtz, Jin Seo Im, Stephen K. Gray,* and Gary P. Wiederrecht*

Chemistry Division, Argonne National Laboratory, Argonne, Illinois 60439

Received: June 23, 2003; In Final Form: September 3, 2003

Near-field scanning optical microscopy (NSOM) is used to explore the optical scattering from isolated metal nanoparticles (MNPs) and arrays of MNPs. The optical excitation source is an evanescent wave created through total internal reflection of a continuous wave laser beam at the sample–air interface. For optical excitation of isolated Ag and Au MNPs, experimental results show that the scattered light propagates into the far field at an angle of 19° from the substrate. Finite-difference time-domain (FDTD) calculations are used to study simpler but related metallic nanowire systems under evanescent wave excitation. The FDTD results are found to be similar to the experimental results, indicating the generality of the scattering phenomenon. NSOM characterization of plasmonic arrays that consist of closely spaced Ag MNPs are subsequently reported. Confined optical signals within the array are observed along with a reduction in the far-field scattered signal. Simultaneous collection of the atomic force microscopy signal and near-field signals also shows that the spatial distribution of the near-field is strongly modified in the arrays compared to isolated MNPs. FDTD studies on arrays of nanowires also show large differences from the isolated metal nanoparticle calculations, including a decrease in the forward scattered angle (with chain length) and diminished overall forward scattering.

Introduction

The interaction of light with metal nanoparticles (MNPs) produces a range of physical and chemical phenomena that impact an extraordinary breadth of basic science research and technological applications. Areas of interest include surface enhanced Raman scattering,[1–3] surface plasmons,[4] molecular sensors,[5] near-field optical applications,[6] and electronic coherences for nanophotonics applications,[7–9] to name only a few. Recent interest in MNP-based structures is particularly driven by advances in chemical synthesis and lithographic techniques that reliably produce complex shapes, narrow size distributions, and hybrid core–shell materials. These efforts make clear that the optical properties of MNPs can be tailored to facilitate a desired photochemical or photophysical response.

While the tunable absorption properties of MNPs are increasingly well-appreciated, the near-field optical scattering of MNPs is not as well understood or as widely studied. This is due to the relatively recent availability of scanning probe techniques, such as near-field scanning optical microscopy (NSOM), that enable the characterization of the near-field spatial profile of a MNP in differing illumination geometries. Precise characterization of these fields will enable nanophotonic and nanoelectronic applications.[10,11] For example, the spatial profile of the near field of MNPs impacts the efficiency of near-field energy exchange in arrays of closely spaced MNP arrays that are of interest for subdiffraction optical waveguides. In these one-dimensional arrays, electromagnetic energy propagation occurs through the propagation of surface plasmon polaritons, which are photon-coupled free-electron oscillations in metals.[12] Recent literature is providing an increasing body of experimental and theoretical support for surface plasmon polariton (SPP) propagation in "plasmonic" nanoparticle arrays.[7–9,12,13]

We report experimental NSOM and computational electrodynamics studies of the optical scattering from isolated MNPs and MNP arrays. Optical excitation occurs with an evanescent wave created through total internal reflection (TIR) of a continuous wave (CW) laser beam at the sample–air interface. For optical excitation of isolated Au and Ag MNPs, experimental results show that a component of the scattered light propagates into the far field at an angle of 19° from the substrate. Finite-difference time-domain (FDTD) calculations[14,15] are performed on a related two-dimensional model and also show forward scattering into air. NSOM characterization of one-dimensional arrays of closely spaced Ag MNPs are subsequently reported. Ag is chosen over Au due to the lower plasmon damping and longer e–e scattering time relative to Au.[16] A reduction in the far-field scattered signal is observed, and well-confined optical signals provide support for the collective behavior of the MNPs. Simultaneous collection of the atomic force microscopy signal and near-field signals also show that the spatial distribution of the near-field is strongly modified in the arrays vs isolated MNPs. Our model computational studies also show that as the number of MNPs is increased, the forward scattering peak tends to smaller angles and the overall forward scattering diminishes.

Experimental Section

Colloidal Au particles were obtained by reducing potassium gold tetrachloride with sodium borohydride in aqueous solution.[17] The concentration of gold salt was doubled in order to shift the size distribution to larger particles that proved to be more suited for our study. The ground-state absorption spectra of the colloidal solutions featured the absorption of the plasmon dipole mode at 525 nm for the Au colloids. After spin coating on a microscope cover slip for the near-field experiments, atomic force microscopy (AFM) images revealed particles with an average diameter of 30 nm in the region of interest.

The metal nanoparticle arrays are created through electron beam lithography. Glass substrates are spin coated by a double layer of polymethyl methacrylate (PMMA) with different

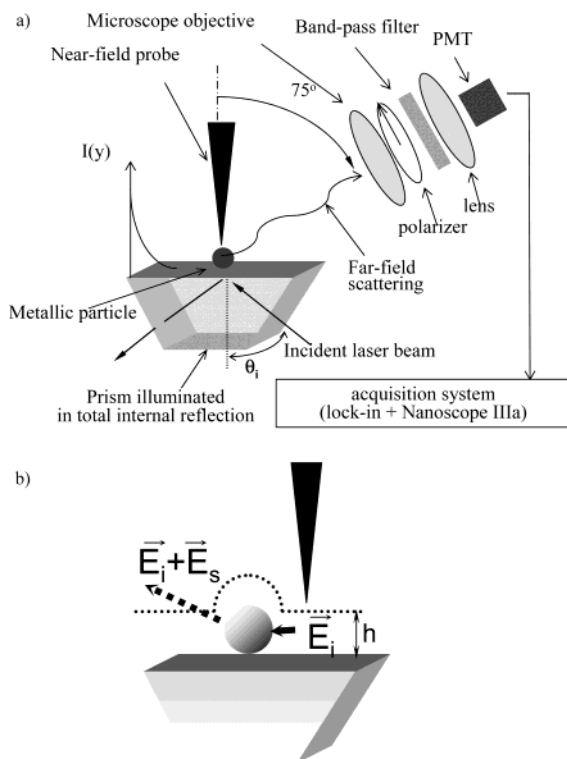* Corresponding authors. E-mail: gray@tcg.anl.gov (S.K.G.); wiederrecht@anl.gov (G.P.W.).

Figure 1. NSOM experimental configuration.

Figure 2. A diagram of the theoretical model. The lower gray region corresponds to glass ($n = 1.5$) and the upper white region corresponds to air ($n = 1$). An electromagnetic wave originating from within the glass region, polarized in the xy plane, and having a propagation vector initially making an angle θ relative to the negative y axis is shown. A metal nanowire, with long cylinder axis in the z direction (out of the plane), is indicated as a filled black circle. The scattering angle, χ, i.e., the angle relative to the positive x axis, is also displayed. The outer hatched regions are where absorbing boundary conditions are applied. Note that this diagram is not drawn to scale.

molecular weights. A thin aluminum layer is deposited on the PMMA to avoid charging effects. After exposure, the aluminum layer is etched by a solution of NaOH followed by development using methyl isobutyl ketone and 2-propanol. Electron beam evaporation is used to deposit a 2-nm Ti layer first, followed by a 40-nm Ag layer. The Ti is utilized to enable the Ag to adhere to the surface. A final polymer liftoff with acetone leaves the MNP patterns.

A diagram of the microscope used for this study is illustrated in Figure 1a. The sample is coupled to a dove prism using immersion oil. The samples are far-field illuminated by an evanescent wave obtained by a slightly focused 10-mW laser beam from a Kr^+ or Ar^+ laser undergoing TIR at the sample$-$air interface (incidence angle $\theta_i = 50°$). A half-wave plate controls the incident polarization; the polarization ratio was measured to be about 400:1 at the prism entrance facet. Under these conditions we measured a ca. 100-nm penetration depth of the evanescent wave above the sample. The 10^{-4} cm^2 illuminated area results in a 100 W/cm^2 power density on the sample surface.

The optical near-field distribution was probed using a commercially available silicon tip (NCH-W, Nanosensors). An atomic force feedback loop (Multimode/Nanoscope IIIa controller, Digital Instruments) ensured a constant probe$-$sample distance regulation in the intermittent contact (tapping) mode. A microscope objective (0.28 NA, 33-mm working distance) collects the field diffracted by the probe$-$sample interaction at an angle of 75° from the probe axis in the backscattering direction with respect to the incident wave vector (see Figure 1a). The polarization of the resulting collimated beam is then analyzed and subsequently focused onto an optical fiber (0.2 NA, 100-μm core diameter) with a 3-cm focal length lens. This confocal-type configuration allows us to spatially isolate a ca. 30-μm diameter area from the focal plane of the microscope objective and thus dedicate the dynamic of our light sensor to the region where the probe is interacting with the sample. The output of the fiber is incident on a photomultiplier tube
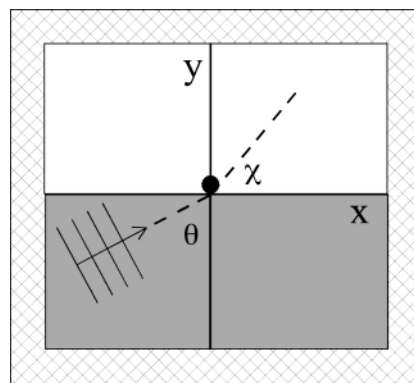
(Hamamatsu H5773-01) via an interference filter centered at 400 ± 25 nm and is lock-in demodulated to provide the NSOM signal. The results presented in this paper were obtained for a probe vibration amplitude of 50 nm and lock-in detection at the probe vibration frequency of ca. 330 kHz or its second harmonic. We also restrict our present analysis to the near-field contrast associated with the intensity of the field component polarized mainly perpendicularly to the substrate. Because of the average collection angle of 75° in Figure 1, a small component of the scattered field polarized parallel to the substrate is also present in the collected light. For experiments designed to determine the far-field scattering angle from the MNPs, the average tip$-$sample separation was gradually increased and assigned a height h.[18] This mode of operation is illustrated in Figure 1b. A value of $h = 0$ means that the average tip$-$sample distance corresponds to the probe's vibration amplitude of 50 nm.

Theoretical Methods

The realistic computational modeling of three-dimensional MNPs over the length scales required to adequately describe TIR experiments such as those described above is challenging. While we do plan to undertake such calculations in the future, we chose to study a related model system of one or more metal nanowires, which is essentially two-dimensional in nature, but includes the main features of the experiments. We imagine a system, schematically drawn in Figure 2, with cylindrical symmetry, e.g., the xy plane with z invariance being assumed. For $y < 0$, we have a dielectric material, and for $y \geq 0$ we have free space. Sitting on top of the dielectric, in free space, we have one or more metallic nanowires with infinite extent along z but some circular radius a in the xy plane.

We consider a two-dimensional system so that only two electric field components, $E_x(x,y,t)$, $E_y(x,y,t)$, and one magnetic field component, $H_z(x,y,t)$ are propagated in time, t, along with extra current density terms, $J_x(x,y,t)$ and $J_y(x,y,t)$, to characterize metallic regions. Let $\mathbf{E} = \mathbf{i}\, E_x + \mathbf{j}\, E_y + \mathbf{k}\, 0$, $\mathbf{H} = \mathbf{i}\, 0 + \mathbf{j}\, 0 + \mathbf{k}\, H_z$, and $\mathbf{J} = \mathbf{i}\, J_x + \mathbf{j}\, J_y + \mathbf{k}\, 0$. Maxwell's equations are

$$\frac{\partial}{\partial t} \mathbf{E}(x,y,t) = \frac{1}{\epsilon_{\text{eff}}(x,y)} [\nabla \times \mathbf{H}(x,y,t) - \mathbf{J}(x,y,t)]$$

Optical Scattering from Nanoparticles and Arrays

J. Phys. Chem. B, Vol. 107, No. 51, 2003 **14193**

$$\frac{\partial}{\partial t} \mathbf{H}(x,y,t) = -\frac{1}{\mu_0} \nabla \times \mathbf{E}(x,y,t)$$

$$\frac{\partial}{\partial t} \mathbf{J}(x,y,t) = \alpha(x,y) \mathbf{J}(x,y,t) + \beta(x,y) \mathbf{E}(x,y,t) \quad (1)$$

In free space, $\epsilon_{\text{eff}} = \epsilon_0$, and in the dielectric region, $\epsilon_{\text{eff}} = 2.25\epsilon_0$, consistent with refractive index $n = 1.5$. In both these regions, $\alpha = \beta = 0$. In a metallic (x,y) region, ϵ_{eff}, α and β take on values characteristic of the metal. If we assume a Drude form[19]

$$\epsilon(\omega) = \epsilon_\infty - \frac{\omega_p^2}{\omega^2 + i\Gamma_p\omega} \quad (2)$$

then[15] $\epsilon = \epsilon_\infty \epsilon_0$, $\alpha = -\Gamma_p$, and $\beta = \epsilon_0 \omega_p^2$. Notice that while the equations of motion, eq 1, do not explicitly involve eq 2, the choices for ϵ_{eff}, α, and β above yield time-domain solutions that are indeed equivalent to the use of eq 2 in the frequency domain, as was demonstrated in the Appendix of ref 15. As in ref 15, we use Drude parameters fit to empirical dielectric constant data in the wavelength region of interest (350−450 nm),[20,21] as opposed to a strict interpretation of the meanings of the parameters within the Drude model. For Ag, we use ϵ_∞ = 8.926, ω_p = 11.585 eV, and Γ_p = 0.203 eV, which yields cross sections in reasonable agreement with those inferred directly from the empirical dielectric data using Mie theory.[19] Specifically, the SPP resonance occurs in the λ = 340−360-nm range for isolated Ag nanowires of diameter ∼100 nm. When placed on top of a glass layer (as in the present study), this SPP resonance redshifts to ∼400 nm. For Au, we determined the parameters ϵ_∞ = 0.25, ω_p = 14.143 eV, and Γ_p = 10.737 eV, also valid for the 300−450-nm region. Note, unlike Ag, Au does not have a SPP resonance in this wavelength region; the Au SPP occurs at somewhat more red-shifted wavelengths in the 450−500-nm range. The SPP positions for nanoscale radius metallic cylinders, which we are discussing here, tend to be slightly (20−40 nm) blue-shifted relative to their spherical MNP counterparts owing to a slight difference in the zero-order SPP resonance condition for cylinders compared to spheres. This can be deduced by direct evaluation of the Mie-type cross sections for spheres and cylinders or by examining the small-particle limiting expressions.[19]

Of course the Drude model, which is consistent with free-electron (intraband) behavior, has limitations.[19,20] For both Ag and Au, it is difficult to obtain a quantitative fit of the dielectric constant data using eq 2 even over the limited 350−450 nm region. For Ag, in this region, our Drude fit is qualitatively correct but tends to exhibit greater deviations from experiment at the higher wavelength (lower frequency) limit. For wavelengths near 400 nm, however, our primary region of interest, the errors are on the order of 20−30% for both the real and imaginary parts. Our Drude fit for Au for wavelengths near 400 nm is accurate to about 20%. It should be noted that the Drude fit for Au does not describe qualitatively the 500 nm wavelength region where interband effects occur and a mixed Drude−Lorentzian model is more appropriate.[19,20]

Equation 2 is discretized in space and time and solved with the FDTD method.[14,15] In our calculations, each of the x and y grids consists of 3 000 evenly spaced points in the range (−2500 nm to +2500 nm). For Ag, about 10 000 small time steps $\Delta t = 3.2 \times 10^{-18}$ s are taken. For Au, somewhat smaller time steps $(\Delta t/2)$ are required to avoid instabilities. After each time step, all the field components are softly damped in the first 400 and last 400 nm of each grid in order to accomplish absorption of

field components that are approaching the grid edges and thus prevent spurious back reflections. In addition to simply inspecting the time variation of the fields, we also compute an angle-resolved scattering intensity in the free space region, associated with a given wavelength, by Fourier transforming (on some wavelength $\lambda = 2\pi c/\omega$ of interest) the time-resolved electric and magnetic field components along a circle of large fixed radius (ran = 2000 nm) centered about the origin or central nanowire and constructing the scattering intensity, $I(\chi) \propto$ the radial component of $\mathbf{E}_\lambda(\chi) \times \mathbf{H}_\lambda^*(\chi)$, with χ being the angle relative to the positive x axis. (The way we construct our initial condition (see below), consistent with TIR, the total and scattered fields are the same in the free-space region of interest.) Each full propagation requires a few hours computation time on a G4 Apple Macintosh computer.

An initial condition must be specified to carry out the propagations and analysis described above. The boundary between the more optically dense medium (for $y < 0$) and free space is the x axis with $y = 0$. As an initial condition, we use a Gaussian-damped plane wave pulse centered at 1000 nm from the $x = y = 0$ origin in the lower left quadrant ($y < 0$, $x < 0$) that moves up through the optically dense medium toward the origin. The full widths at half maximum in both the x and y directions of the pulse are 500 nm, and the central wavelength is $\lambda \approx 400$ nm. The central wave vector is $\mathbf{k} = \mathbf{i} k_x + \mathbf{j} k_y$ with components k_x and k_y such that $\mathbf{k}$ makes an angle, θ, with the negative y axis that exceeds the critical angle, θ_c. In this case, TIR might be expected to occur in the absence of any nanoparticles sitting on the boundary. For $n = 1.5$, $\theta_c = \sin^{-1}(1/1.5) = 41.8°$. We use a $\mathbf{k}$ vector with $\theta = 50°$ relative to the negative y axis, thus exceeding θ_c. Actually, an interesting technical problem arises because of the finite nature of the initial pulse. While a true, infinitely extended plane wave or superposition of such waves all with $\mathbf{k}$ vectors such that $\theta > \theta_c$ will exhibit TIR, a finite-sized pulse formed from a plane wave with $\mathbf{k}$ vector satisfying $\theta > \theta_c$ will contain a range of $\mathbf{k}$ vectors and some of these may have $\theta < \theta_c$. One could attempt to subtract out, analytically, such undesired components. However a simpler device, exploiting the time-reversal symmetry of Maxwell's equations, is to propagate the initial condition discussed above and after some suitable time visually inspect the electromagnetic fields and identify the unwanted refracting components (generally in the upper right quadrant, $x > 0$, $y > 0$). One then can simply set to zero these components and propagate the new system *backward* in time to $t = 0$. The result is a new initial pulse that, when propagated forward in time, will not refract into the free space region and will exhibit TIR.

Results and Discussion

Representative experimental images from simultaneous AFM and NSOM measurements of isolated Au MNPs are shown in Figure 3. The particle is approximately 25 nm in diameter and is excited in transverse magnetic polarization. As h is increased, the field observed in the NSOM experiments is shown to spread in the forward scattering direction and to have a "V"-shaped distribution. Following the lateral displacement of the point of maximum intensity as h is increased vs the position of the particle, we can deduce the far-field scattering angle. Note that this maximum occurs in the plane of incidence, making the results of the two-dimensional FDTD calculations (made in the plane of incidence) presented in the next paragraph relevant for comparison. Figure 4 shows the scattering angle with respect to the surface plane vs the height. According to Figure 4, the angle increases with height up to 120 nm, at which point it
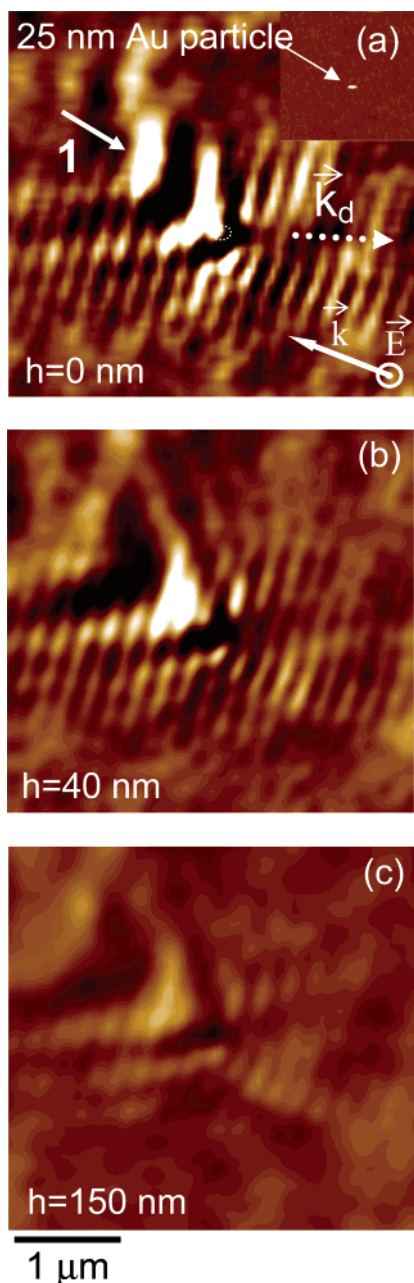
Figure 3. NSOM images of a Au MNP illuminated in TIR at 415.4 nm on a glass substrate at varying values of h. The direction and polarization of the incident wave are indicated by $(\vec{k}, \vec{E})$. k_d represents the projection on the surface of the detected scattered signal.

Figure 4. The scattering angle calculated from the lateral displacement of the point of maximum intensity as a function of height for the Au MNP. The error bars represent 10% of the calculated data. Filled symbols denote actual data and the line provides a guide for the eyes.

Figure 5. The calculated far-field scattering intensity at 400 nm vs angle for 100 nm diameter Au and Ag nanowires using FDTD simulations.

adopts asymptotical behavior at the angle of ca. 19°. A lack of contrast in the NSOM images above $h = 150$ nm prohibits further measurements. This value is in excellent agreement with earlier theoretical predictions as well as recent experimental results showing a similar behavior for the diffraction of a surface-plasmon polariton wave by an individual surface defect.[22−24] Accordingly, our results show that an evanescent Fresnel wave can be scattered away from the surface in the far-field by a particle of nanometric size. Moreover, this set of images demonstrates that nonpropagating scattering is not the only contribution to the contrast of Figure 3a where the radiative mode is labeled with arrow 1. The consequence of that is clearly shown in Figure 4 where the strong variation of the scattering angle χ in the 0−140-nm range is the result of the contribution of a broad spectrum of evanescent waves to the scattered intensity. The sensitivity of our measurements to the progressive
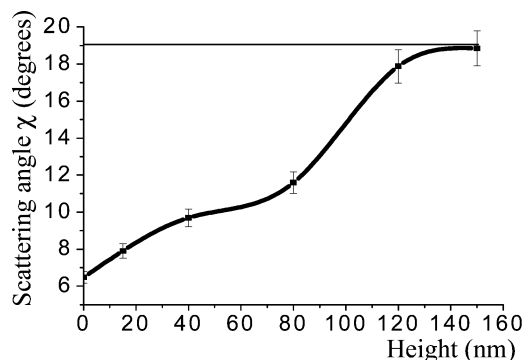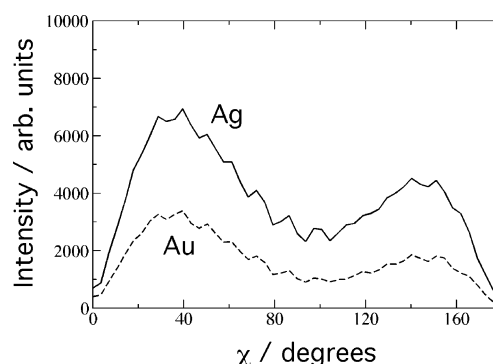
mode only would result in a constant measured angle at $\chi = 19°$ vs height in Figure 4 as this field component is propagating in free space. The detailed origin of the contrast in Figure 3 is beyond the scope of this paper and will be discussed elsewhere.

FDTD calculations, as described in the Theoretical Methods above, were carried out to gain insight into the results shown in Figures 3 and 4. In the case of Au, we examined nanowires with diameters of 25, 50, and 100 nm. The results for *all* diameter sizes were qualitatively very similar with, as might be expected, the scattering intensity increasing with particle diameter. Figure 5 shows the resulting angle-resolved light scattering intensity (for $\lambda = 400$ nm) for 100-nm diameter Au nanowires as a dashed curve. Scattering angles $0 \leq \chi < 90°$ correspond to forward scattering into the $x > 0$, $y > 0$ quadrant. A peak is evident in the scattering intensity near $\chi = 35°$. This is higher than the experimentally observed 19° scattering angle but is qualitatively consistent with experiment. Figure 5 also shows the corresponding results for a 100-nm diameter Ag nanowire (solid curve). The intensity in this case is larger than that for Au owing to the light being closer to the Ag SPP resonance, which is near 400 nm in this case. This shows that the nature of the underlying MNP material is important for the intensity of scattering, but not necessarily the qualitative form of the far-field angular distribution.

Notice that Figure 5, for both Au and Ag, also shows a somewhat less intense, larger angle scattering peak near 140°. It is natural to term this behavior "backscattering". (The reader should keep in mind that it is backscattering in relation to the incident wave vector of the incident evanescent wave vector that is moving along the interface.) Figure 3 does not demonstrate such backscattering behavior because both radiated modes are not equivalently characterized in the fixed solid angle in
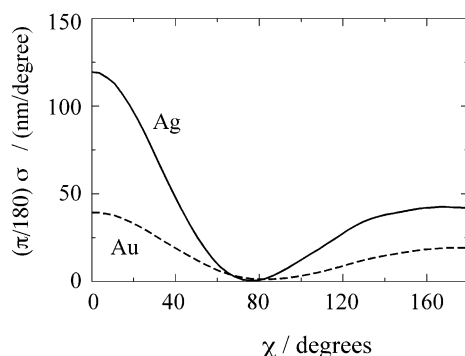
Optical Scattering from Nanoparticles and Arrays

J. Phys. Chem. B, Vol. 107, No. 51, 2003 **14195**

Figure 6. Angular scattering cross sections for Ag and Au cylinders (or nanowires) in free space. The cylinder diameters are 100 nm and the incident light has $\lambda = 350$ nm exciting the Ag nanowire resonantly. Relative to Figure 2, the incident light is simply y polarized and moving from left to right along the x axis.

which we analyze the field scattered by the probe (see Figure 1). Thus, in Figure 3 for the forward scattered mode, the field backscattered by the probe is analyzed. In this case, although the NSOM contrast results from a convolution of both the sample and the probe scattering cross sections, the probe is assumed to behave passively and Figure 3 represents primarily the field diffracted by the nanoparticle. For the particle's far-field backscattered mode, the situation is drastically different as this mode is analyzed through the probe's forward scattering diffraction pattern. In this case, we showed that this progressive component of the particle's field is radiated at grazing angle by the probe[25] and that the corresponding NSOM contrast is related to the far-field scattering diagram from a cone, i.e., the optical properties of the probe are observed rather than those of the nanoparticle.[25,26]

The form of the scattering intensity for single Ag or Au nanowires on a glass substrate, Figure 5, is somewhat related to the corresponding isolated nanowire results without a substrate. The TIR excitation process, as we will see in the detailed time snapshots below, involves excitation of the nanowire by an evanescent wave which, apart from the exponential decaying component along y, bears some similarity with y-polarized light moving from left to right along the x axis. The analytical solution for the case of small particle radii $a \ll \lambda$ is consistent with light interacting with an oscillating dipole, and the scattering cross sections are proportionate to $\cos^2(\chi)$.[19] Actually this limit is not quantitative in the present case but is still more or less qualitatively correct. We have calculated, using the methods of ref 15, the angle-resolved scattering cross sections for 100-nm diameter Ag and Au nanowires interacting with y-polarized incident light of wavelength $\lambda = 350$ nm, near the isolated Ag nanowire surface plasmon resonance and display the results in Figure 6. (One of course could also use the somewhat complex analytical formulas of ref 19. However, ref 15 showed the FDTD numerical procedure to be accurate.) One sees, for both Ag and Au nanowires in free space, two lobes, a strong forward peak centered at $\chi = 0°$ and a somewhat weaker, broader backward-scattering peak centered at $\chi = 180°$. One view of the effect of placing the nanowires on a glass substrate is to lead, effectively, to a distortion of these lobes away from their $\chi = 0°$ and $\chi = 180°$ centers into something more like the result seen in Figure 5. (Actually, the scattering into the glass medium shows lobes, rather distorted from those in Figure 5, that are consistent with a bifurcation of the original, free-space lobes.) Note that Figure 6 also serves to further show that the surface plasmon excitation, which is being excited in the Ag case and not in the Au case, leads to an increase in the scattering
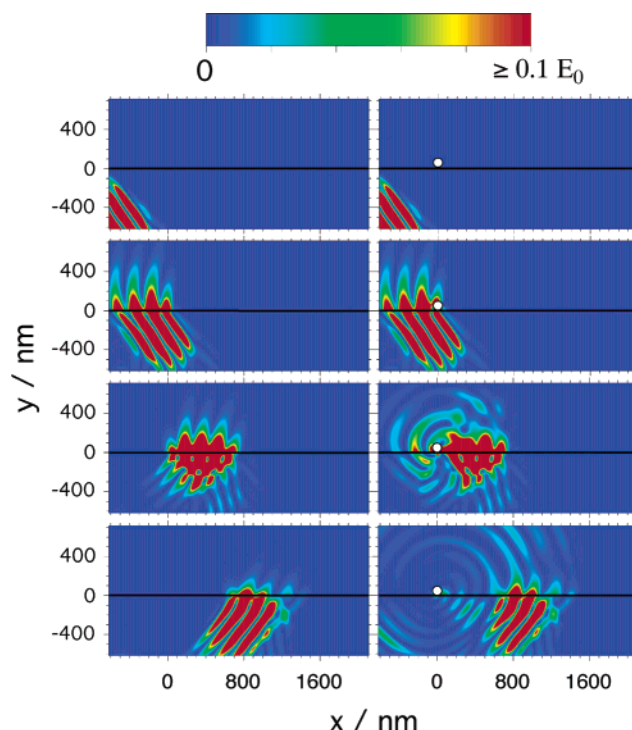

Figure 7. Time sequences of the magnitude of the electric field from FDTD simulations. In all panels, $y > 0$ corresponds to refractive index $n = 1$, $y < 0$ corresponds to $n = 1.5$, and a solid line is shown to mark the interface. The four panels on the left, top to bottom, show a pulse of light emanating from the lower left quadrant of the $n = 1.5$ medium, traveling up toward the interface at $y = 0$, and undergoing internal reflection back into the medium. The time interval between panels is about 2.6 fs. The four panels on the right correspond to the same situation except now a 100 nm diameter Ag nanowire has been placed on top of the $n = 1.5$ medium near the origin. To see the scattered light clearly, we use a color scale such that blue is zero field and red corresponds to field magnitudes greater than or equal to 0.1 E_0, where E_0 is the incident maximum strength.

intensity but not a significant change of the qualitative form of the scattering distribution. However, the calculations show that there is an increase in the forward scattering vs backscattering when the particle is excited on resonance, which is consistent with the higher scattering cross section of Ag in Figure 6.

It is instructive to examine the time evolution of the electric field associated with our calculations. The results for Au and Ag are similar and Figure 7 displays the particular result for 100-nm diameter Ag nanowires. Figure 7 shows a time sequence of the magnitude of the electric field. The top-left panel of Figure 7 shows the electric field in the $n = 1.5$ medium, just about to encounter the interface with free space. The middle-left panels show the development of the evanescent wave, and the bottom-left panel shows it being reflected back into the $n = 1.5$ medium. The situation with the Ag nanowire present is indicated on the right-hand panels of Figure 7. Low-angle scattering into free space is evident in the middle-right panels. (We have placed a white circle over the region occupied by the nanowire to aid in the visualization.) The right-hand side panels of Figure 7 show that light first tends to backscatter and then forward scatter, corresponding to the peaks we observe in Figure 5. We carried out comparable calculations with an Au nanowire. Similar scattering was observed, but it was less intense.

We now turn to the experimental AFM and NSOM results for one-dimensional arrays of Ag MNPs. The arrays consists of 100-nm diameter Ag particles that are spaced by 200 nm center−center. The particles are approximately 40 nm high. Typical results are shown in Figures 8 and 9. Note that these
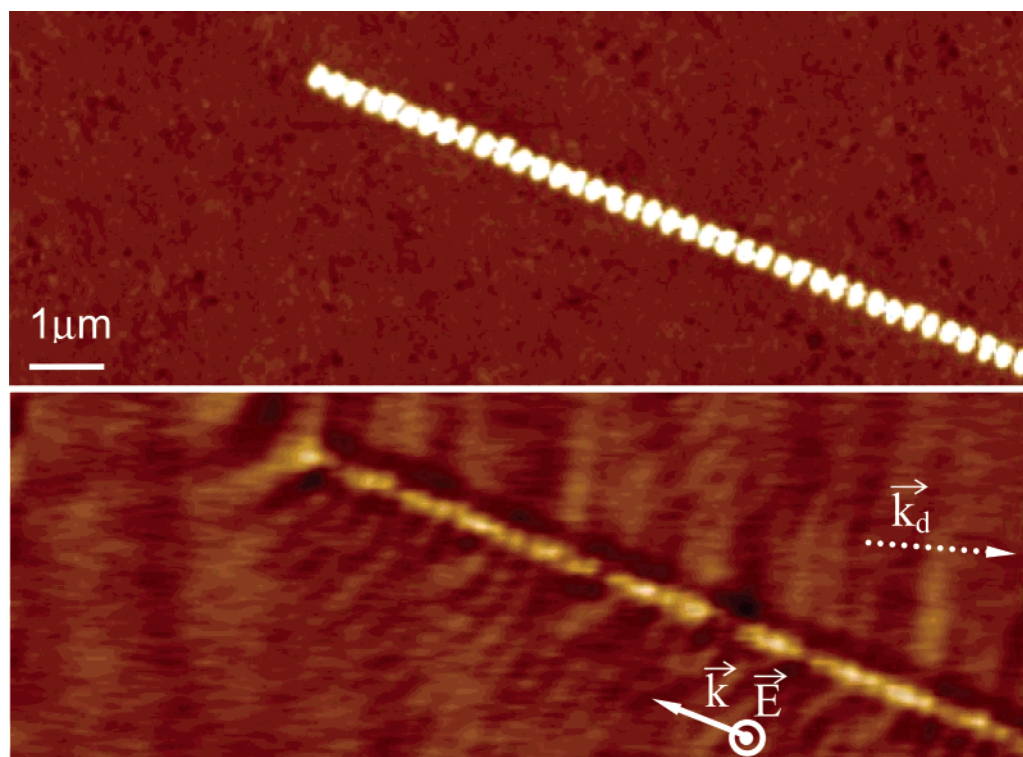
Figure 8. AFM (top) and NSOM (bottom) data for a one-dimensional chain of Ag MNPs excited at $\lambda = 415.4$ nm is shown, demodulated at the first harmonic of the AFM cantilever frequency.

arrays were chosen based on the best contrast for the discussed effects and represent differently shaped particles, and therefore different illumination wavelengths are utilized in their characterization (415 and 488 nm, respectively). In general, small changes in the intensity and spatial distribution of the near-field contrast are observed at different wavelengths and polarization in the 400−500-nm range. Figure 8 shows the NSOM data that is collected with a lock-in frequency equal to that of the cantilever frequency, while Figure 9 shows the data that is demodulated at twice the cantilever frequency. The use of higher harmonic detection with apertureless NSOM has the effect of favoring spatially nonlinear fields, so that the fields of a more confined nature are preferentially observed.[27,28] Figure 8 illustrates clearly the forward scattered field, though significantly reduced in contrast relative to that of the isolated MNPs. Figure 9 shows the confined near-field response of the nanoparticle array to photoexcitation. Overlap of the topographic AFM image and the NSOM image shows a slight displacement of the near-field maxima in the forward-scattering direction relative to the Ag nanoparticle. Interestingly, there is a wide distribution in the shape and intensity of the near-field signal. Some particles in fact appear to be missing any near-field contrast. This is likely due to the sensitivity of near-field energy exchange on shape and size defects of the individual particles. Such defects can alter both the spectral and spatial scattering properties of the particle and thus eliminate the possibility of collective interaction with a neighboring nanoparticle.

A variety of FDTD calculations were performed for analogous chains of Ag nanowires. We examined chains of up to eight nanowires, with diameter 100 nm and center−center displacement (along x) of 200 nm. (The centers of the nanowires all have $y = 50$ nm and are placed along the x axis with $x = 0$, 200 nm, ...) We still find forward scattering, although it shifts to smaller scattering angles. Figure 10 contrasts our results for one nanowire (solid curve) and eight nanowires (dashed curve). The eight-nanowire case shows a forward-scattering angle of

just 10° compared to 35° for what we obtained with one nanowire. In terms of integrated intensity from 0 to 90°, say, the forward scattering of the eight-nanowire case is about half as much as the one-nanowire case. Interestingly, backscattering is much more intense in the eight-nanowire case. (Similarly as for the single nanoparticle study, the backscattered mode from the nanoparticle array is not equivalently detected in our experiments.) The backscattering is very sensitive to the details of the nanowire array. For example, if we decrease the separation of the centers from 200 to 150 nm, we obtain a result very similar to the eight-nanowire result of Figure 10 except that the magnitude of the backscattering peak is considerably lowered to being a factor of 4 less than the forward scattering peak. It is the small-angle forward-scattering peak that remains reasonably robust and is, in our view, the more interesting feature. This is because it represents light energy moving along the nanowire array and emanating out from near the end of the array.

Finally we should note that there are some interesting similarities of the problems studied here and Kretschmann-attenuated total-reflection studies of surface plasmons in metallic films.[22−24,30−33] In these studies, laser light coming up through the prism excites propagating surface plasmon modes in the metallic film which in turn can be scattered back into photons by defects in the film. The conical scattering of light back down into the prism medium is one focus of the work of Ketterson and co-workers.[32,33] A dispersion relation for propagating surface plasmons, coupled with momentum conservation allows for a simple rationalization of the main features of the conical radiation.[30−33] For example, an optimal angle of incidence consistent with exciting the propagating surface plasmons in the film can be deduced, which also relates to the shape of the scattered cone into the hemispherical glass prism. Our situation is obviously not exactly the same; we have one or more isolated MNPs sitting on the glass surface, and we have been concerned with the scattering of light into air. However, it may be possible to borrow some of the approximate methods of analysis. For
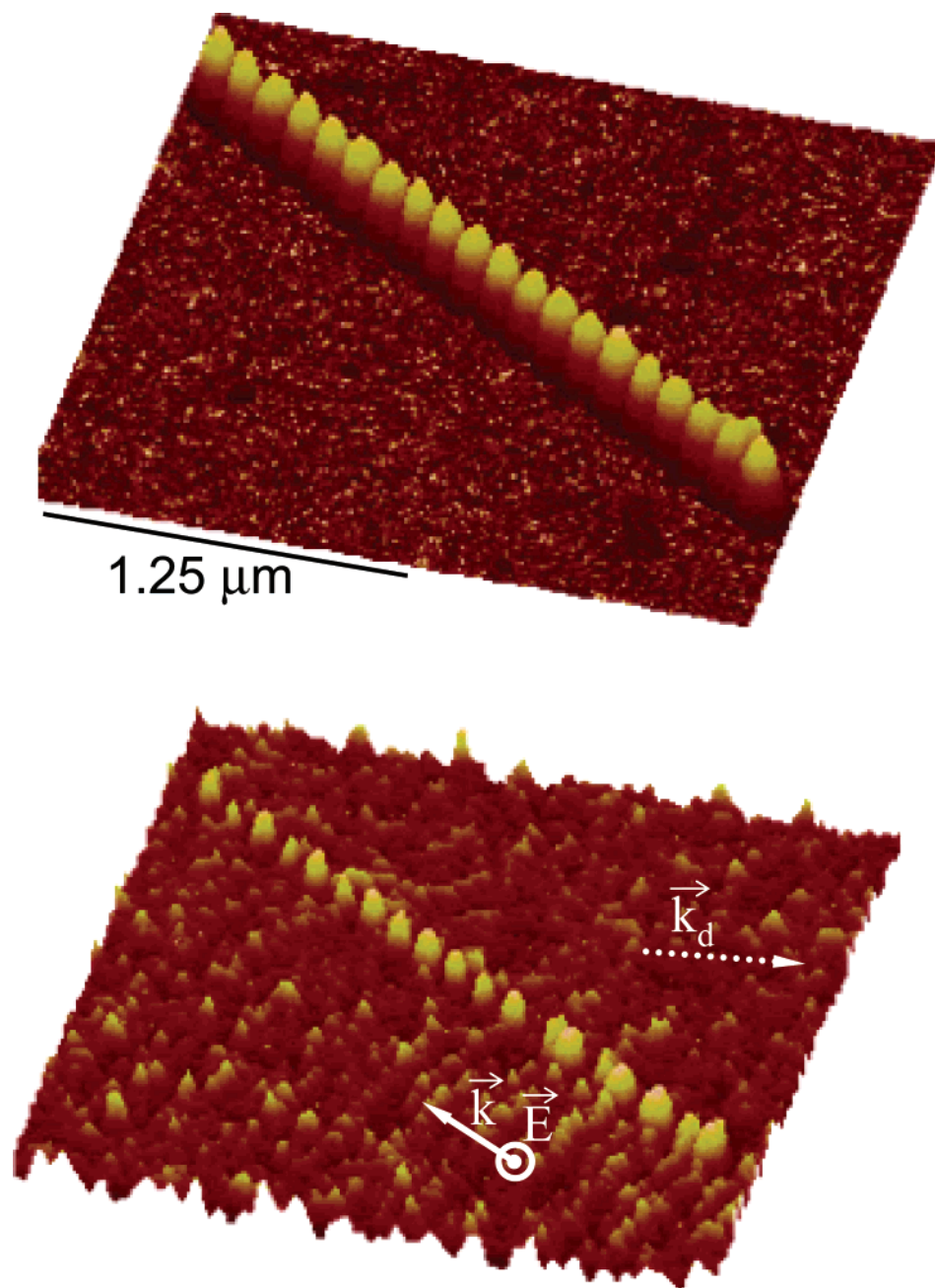
Optical Scattering from Nanoparticles and Arrays

J. Phys. Chem. B, Vol. 107, No. 51, 2003 **14197**

Figure 9. AFM (top) and NSOM (bottom) data for a one-dimensional chain of Ag MNPs excited at $\lambda = 488$ nm is shown, demodulated at the second harmonic of the cantilever frequency.

example, the multiple-scattering analysis ideas of ref 33 that involve waves scattering and interfering from various surface defects could be used to analyze MNP arrays such as we studied here. The backscattering noted in the previous paragraph could possibly be explained by such considerations and related ideas involving diffraction. While our array systems are finite and the simplest diffraction formulas do not rigorously apply, it may still be the case that, effectively the incident light couples to electromagnetic modes of the system that are related to the incident wave vector by multiples of $2\pi/d$, where d is the center−center spacing.[34,35] Nonradiative (e.g., absorption) aspects of some of these modes may also come into play in lowering the far-field scattering. A more extensive theoretical/computational study of these points would be very interesting.

Conclusions

We have studied the near-field optical response of isolated and one-dimensional chains of noble MNPs excited by an evanescent wave. NSOM studies clearly show that the scattering of the light into the far field occurs at an angle of approximately 19° from the substrate for isolated particles. The arrays, however, show a dramatically reduced level of far-field scattering and enhanced near-field contrast. The structural sensitivity of the light scattering indicates that these nanophotonic structures could be useful as chemical or biological sensors.[29] Computational electrodynamics studies on related metal nanowires also find a forward scattering angle peak, although at a larger angle closer to 35°. These results also showed that the scattering is enhanced if the wavelength of light is closer to the surface plasmon resonance. The corresponding calculations on arrays of nanowires showed smaller-angle forward scattering, which represents a promising indicator of waveguiding properties.

Future experimental efforts will focus on the wavelength and polarization dependence of metallic waveguides as a function of their geometry and material. In this vein, efforts are ongoing to improve the quality of the arrays obtained through electron
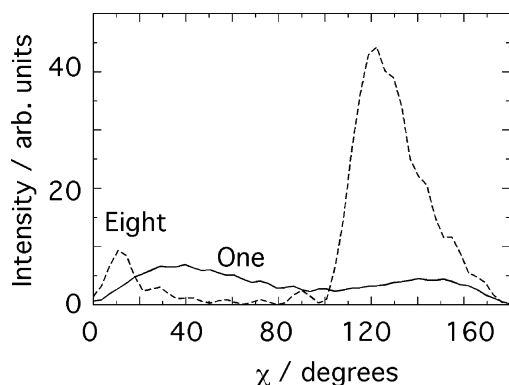
Figure 10. Scattering intensity for a chain of eight 100 nm diameter Ag nanowires, centered at $x = 0$, 200 nm, ..., 1400 nm ($y = 50$ nm), dashed curve. The result for one nanowire centered at $x = 0$, $y = 50$ nm (same result as in Figure 5) is also indicated as a solid curve for comparison.

beam lithography, critical to the waveguiding properties. We also plan to extend the FDTD calculations to three dimensions, especially including the probe, to connect more directly with the experimental studies. These efforts will also enable us to investigate some of the more general, interpretative issues raised toward the end of the last section.

References and Notes

(1) Moskovits, M. *Rev. Mod. Phys.* **1985**, *57*, 783.
(2) Schatz, G. *Acc. Chem. Res.* **1984**, *17*, 370.
(3) Campion, A.; Kambhampati, P. *Chem. Soc. Rev.* **1998**, *4*, 241.
(4) El-Sayed, M. A. *Int. Rev. Phys. Chem.* **2000**, *19*, 409.
(5) Park, S.; Yang, P.; Corredor, P.; Weaver, M. J. *J. Am Chem. Soc.* **2002**, *124*, 2428.
(6) Krug, J. T.; Sánchez, E. J.; Xie, X. S. *J. Chem. Phys.* **2002**, *116*, 10895.
(7) Maier, S. A.; Brongersma, M. L.; Atwater, H. A. *Appl. Phys. Lett.* **2001**, *78*, 16.

(8) Maier, S. A.; Brongersma, M. L.; Kik, P. G.; Meltzer, S.; Requicha, A. A. G.; Atwater, H. A. *Adv. Mater.* **2001**, *13*, 1501.
(9) Krenn, J. R.; Dereux, A.; Weeber, J. C.; Bourillot, E.; Lacroute, Y.; Goudonnet, J. P.; Schider, G.; Gotschy, W.; Leitner, A.; Aussenegg, F. R.; Girard, C. *Phys. Rev. Lett.* **1999**, *82*, 2590.
(10) Ohtsu, M.; Kobayashi, K.; Kawazoe, T.; Sangu, S.; Yatsui, T. *IEEE J. Quantum Electron.* **2002**, *8*, 839.
(11) Michaels, A. M.; Jiang, J.; Brus, L. *J. Phys. Chem. B* **2000**, *104*, 11965.
(12) Maier, S. A.; Kik, P. G.; Atwater, H. A.; Meltzer, S.; Harel, E.; Koel, B. E.; Requicha, A. A. G. *Nat. Mater.* **2003**, *2*, 229.
(13) Quinten, M.; Leitner, A.; Krenn, J. R.; Aussenegg, F. R. *Optics Lett.* **1998**, *23*, 1331.
(14) Taflove, A.; Hagness, S. C. *Computational Electrodynamics: The Finite-Difference Time-Domain Method, Second Edition*; Artech House: Boston, 2000.
(15) Gray, S. K.; Kupka, T. *Phys. Rev. B* **2003**, *68*, 045415.
(16) Maier, S. A.; Kik, P. G.; Atwater, H. A. *Appl. Phys. Lett.* **2002**, *81*, 1714.
(17) Kometani, N.; Tsubonishi, M.; Fujita, T.; Asami, K.; Yonezawa, Y. *Langmuir* **2001**, *17*, 578.
(18) Hecht, B.; Bielefeldt, H.; Inouye, Y.; Pohl, D. W.; Novotny, L. *J. Appl. Phys.* **1997**, *81*, 2492.
(19) Bohren, C. F.; Huffman, D. R. *Absorption and Scattering of Light by Small Particles*; Wiley: New York, 1983.
(20) Johnson, P. B.; Christy, R. W. *Phys. Rev. B* **1972**, *6*, 4370.
(21) Lynch, D. W.; Hunter, W. R. *Handbook of Optical Constants of Solids*; Academic: Orlando, 1985.
(22) Sánchez-Gil, J. A. *Appl. Phy. Lett.* **1998**, *73*, 3509.
(23) Sánchez-Gil, J. A.; Maradudin, A. A. *Phys. Rev. B* **1999**, *60*, 8359.
(24) Vohnsen, B.; Bozhevolnyi, S. I. *Appl. Opt.-LP* **2001**, *40*, 6081.
(25) Wurtz, G. A.; Dimitrijevic, N. M.; Wiederrecht, G. P. *Jpn. J. Appl. Phys.* **2002**, *41*, L351.
(26) H'dhili, F.; Bachelot, R.; Lerondel, G.; Barchiesi, D.; Royer, P. *Appl. Phys. Lett.* **2001**, *79*, 4019.
(27) Walford, J. N.; Porto, J. A.; Carminati, R.; Greffet, J.-J.; Adam, P. M.; Hudlet, S.; Bijeon, J.-L.; Stashkevich, A.; Royer, P. *J. Appl. Phys.* **2001**, *89*, 5159.
(28) Knoll, B.; Keilmann, F. *Opt. Commun.* **2000**, *182(4−6)*, 321.
(29) Cao, Y. W. C.; Jin, R. C.; Mirkin, C. A. *Science* **2002**, *297*, 1536.
(30) Braundmeier, A. J., Jr.; Tomaschke, H. E. *Opt. Commun.* **1975**, *14*, 99.
(31) Simon, H. J.; Guha, J. K. *Opt. Commun.* **1976**, *18*, 391.
(32) Kim, Y.-K.; Auvil, P. R.; Ketterson, J. B. *Appl. Opt.* **1997**, *36*, 841.
(33) Auvil, P. R.; Ketterson, J. B.; Kim, Y.-K.; Kryukov, A. *Appl. Opt.* **1998**, *37*, 8448.
(34) Cottam, M. G.; Tilley, D. R., *Introduction to Surface and Superlattice Excitations*; Cambridge University Press: Cambridge, 1989; pp 218−220.
(35) Popov, E. Light Diffraction by Relief Gratings: A Macroscopic and Microscopic View. In *Progress in Optics*; Wolf, E., Ed.; Elsevier Science: 1993; Vol. 31.